Extreme events driving year-to-year differences in gross primary productivity across the US

Alexander J. Turner[1,2,3]*, Philipp Köhler[4], Troy S. Magney[5],
Christian Frankenberg[4,3], Inez Fung[1], and Ronald C. Cohen[1,2]

[1]Department of Earth and Planetary Sciences, University of California, Berkeley, CA, 94720, USA.
[2]College of Chemistry, University of California, Berkeley, CA, 94720, USA.
[3]Jet Propulsion Laboratory, California Institute of Technology, Pasadena, CA, 91109, USA.
[4]Division of Geological and Planetary Sciences, California Institute of Technology, Pasadena, CA, 91226, USA.
[5]Department of Plant Sciences, University of California, Davis, CA, 95616, USA.

Key Points:

- We estimate 500-m GPP from TROPOMI SIF over a moving 16-day window for all of the conterminous United States.
- There are two distinct relationships between TROMPOMI SIF and AmeriFlux GPP across ecosystems.
- Extreme precipitation events drive four regional GPP anomalies that account for 28% of the year-to-year differences across the US.

---

*now at: Department of Atmospheric Sciences, University of Washington, Seattle, WA, 98195, USA

Corresponding author: Alexander J. Turner, `turneraj@uw.edu`

Abstract

Solar-Induced chlorophyll Fluorescence (SIF) has previously been shown to strongly correlate with gross primary productivity (GPP), however this relationship has not yet been quantified for the recently launched TROPOspheric Monitoring Instrument (TROPOMI). Here we use a Gaussian mixture model to develop a parsimonious relationship between SIF from TROPOMI and GPP from flux towers across the conterminous United States (CONUS). The mixture model indicates the SIF-GPP relationship can be characterized by a linear model with two terms. We then estimate GPP across CONUS at 500-m spatial resolution over a 16-day moving window. We find that CONUS GPP varies by less than 4% between 2018 and 2019. However, we observe four extreme precipitation events that induce regional GPP anomalies: drought in west Texas, flooding in the midwestern US, drought in South Dakota, and drought in California. Taken together, these events account for 28% of the year-to-year GPP differences across CONUS.

Plain Language Summary

Gross primary productivity is the total amount of CO_2 taken up by plants during photosynthesis and represents one of the main drivers of variability in atmospheric CO_2. Plants emit a small amount of light during the process of photosynthesis, this is known as "solar-induced chlorophyll fluorescence" (SIF). We can measure this SIF signal from space and use it to study the biosphere. Here we build a high-resolution estimate of gross primary productivity over the United States using satellite measurements of SIF from 2018 through 2019. We find the major drivers of variability in gross primary productivity across the US were drought in west Texas, flooding in the midwestern US, drought in South Dakota, and drought in California.

1 Introduction

Terrestrial gross primary productivity (GPP) is the total amount of carbon dioxide (CO_2) assimilated by plants through photosynthesis and represents one of the main drivers of interannual variability in the global carbon cycle (Le Quéré et al., 2018). As such, quantifying the spatiotemporal patterns of terrestrial GPP is critical to understanding how the carbon cycle will both respond to and influence climate. Work over the past decade has shown satellite measurements of solar-induced chlorophyll fluorescence (SIF) to correlate strongly with tower-based estimates of GPP (e.g., Frankenberg et al., 2011; X. Yang et al., 2015; Sun et al., 2017; Turner et al., 2020; Wang et al., 2020) and are often used as a remote-sensing proxy for GPP.

This relationship between SIF and GPP is typically expressed through a pair of light use efficiency models (Monteith, 1972) that relate GPP and SIF to the absorbed photosynthetically active radiation (APAR):

$$\text{GPP} = \text{APAR} \times \Phi_{\text{CO}_2} \tag{1}$$
$$\text{SIF} = \text{APAR} \times \beta\Phi_{\text{F}} \tag{2}$$

where Φ_{CO_2} is the light use efficiency of CO_2 assimilation, Φ_{F} is the fluorescence yield, and β is the probability of fluoresced photons escaping the canopy. Solving for APAR and substituting, we can rewrite GPP as:

$$\text{GPP} = \frac{\Phi_{\text{CO}_2}}{\beta\Phi_{\text{F}}}\text{SIF}. \tag{3}$$

The derivation follows from Lee et al. (2013), Guanter et al. (2014), Sun et al. (2017), and others.

This seemingly straight forward relationship between SIF and GPP has been widely used to infer GPP from measurements of SIF (e.g., Frankenberg et al., 2011; Parazoo

et al., 2014; X. Yang et al., 2015; H. Yang et al., 2017; Sun et al., 2017, 2018; Magney et al., 2019; Turner et al., 2020) with some work showing that SIF captures more variability in GPP than APAR alone (e.g., X. Yang et al., 2015; H. Yang et al., 2017; Magney et al., 2019). However, there is much complexity encapsulated in the first term of Eq. 3 ($\Phi_{CO_2}/\beta\Phi_F$). There is an ongoing debate about what *exactly* SIF is telling us about GPP (e.g., Dechant et al., 2020; Marrs et al., 2020) and the spatio-temporal scales at which SIF and GPP correlate well.

Here we focus on the ecosystem-scale relationship between SIF and GPP, as that is the relevant observable scale from space-borne instruments. We begin by characterizing the relationship between SIF from TROPOMI and GPP from flux towers. Following this, we use this ecosystem-scale relationship to infer GPP at a spatial resolution of 500-m using TROPOMI SIF measurements and identify drivers of interannual variability in GPP. Previous work has identified effects such as seasonal redistribution (Butterfield et al., 2020), drought (e.g., Sun et al., 2015), and flooding (Yin et al., 2020) as important drivers of interannual variability in GPP.

2 Identifying distinct relationships between SIF and GPP

We build on our previous work (Turner et al., 2020) downscaling measurements of SIF to 500-m spatial resolution. Briefly, the TROPOspheric Monitoring Instrument (TROPOMI; Veefkind et al., 2012) is a nadir-viewing imaging spectrometer. TROPOMI has a 2,600 km swath with a nadir spatial resolution of 5.6 km along track and 3.5 km across track. Köhler et al. (2018) presented the first retrievals of SIF from TROPOMI. As in Turner et al. (2020), we apply a *post hoc* bias correction to ensure positivity of monthly average values as systematically negative SIF values are non-physical. We downscale individual TROPOMI scenes using the near-infrared reflectance of vegetation index (NIR_v) that was proposed by Badgley et al. (2017, 2019). We use the MCD43A4.006 (v06) MODIS NBAR reflectances (Schaaf et al., 2002) to compute NIR_v. Two notable differences from Turner et al. (2020) are: 1) the analysis is extended to cover all of CONUS and 2) we now use a 16-day moving window, thus including a full orbit cycle in each averaging window to minimize effects due to viewing-illumination geometry and noise.

The extension to CONUS facilitates comparison of TROPOMI SIF retrievals to flux tower data over a more representative set of ecosystems and robustly infer the SIF-GPP relationship. Specifically, there are 82 AmeriFlux sites (D. Baldocchi et al., 2001) within CONUS that reported data in 2018, 2019, or 2020 whereas Turner et al. (2020) only included 11 sites and did not have data from forests. Figure 1 shows the location of these 82 AmeriFlux sites overlaid on the dominant landcover. These eddy covariance sites provide a direct measure of net ecosystem exchange (NEE; CO_2 fluxes) (D. D. Baldocchi et al., 1988). We use GPP that has been partitioned by the group operating the site. If GPP is not provided we compute it using nighttime measurements of NEE as a proxy for ecosystem respiration (Reichstein et al., 2005). The AmeriFlux sites used here cover 10 ecosystems as defined by the International Geosphere-Biosphere Programme: evergreen needleleaf forest, deciduous broadleaf forest, mixed forest, grassland, cropland, wetland, woody savanna, savanna, open shrubland, and closed shrubland.

We characterize the relationship between TROPOMI SIF and AmeriFlux GPP by plotting downscaled instantaneous SIF observations against the nearest AmeriFlux GPP data in time. Specifically, the 6 steps we take here are: 1) apply the *post hoc* bias correction to the TROPOMI SIF data, 2) find all TROPOMI scenes that cover an AmeriFlux site, 3) downscale TROPOMI scenes to 500-m using MODIS NIR_v, 4) construct a timeseries of SIF observations from the 500-m grid cell that contains the AmeriFlux site, 5) construct a timeseries of AmeriFlux GPP data that are coincident in time with the TROPOMI overpass, and 6) regress SIF on GPP with a bisquare regression. The bisquare regression was chosen due to robustness against outliers. Additionally, we force the re-
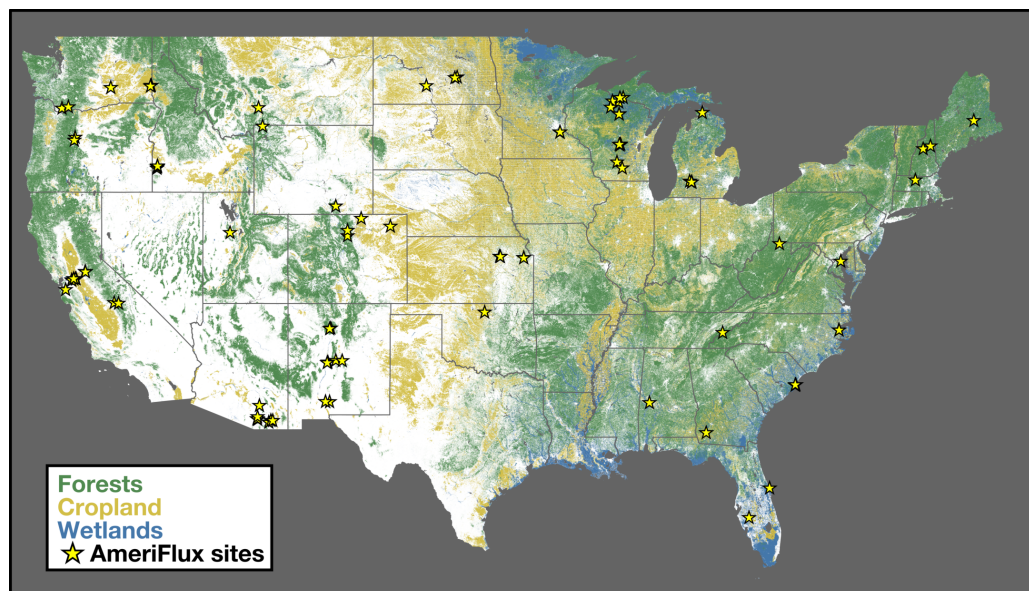
Figure 1. **Dominant landcover over conterminous United States (CONUS).** Colors show the dominant landcover over CONUS. Classification is based on the 2019 USDA CropScape database (USDA, 2018). Forests are shown in green croplands in yellow, and wetlands in blue. Location of 82 AmeriFlux sites used in this study are shown as yellow stars.

gression through the origin based on the physical constraint that GPP should be zero if SIF is zero. We observe a linear relationship between SIF and GPP when plotted against all ecosystems (Supplemental Figure S1) and when separated by ecosystem (Supplemental Figure S2). Notable exceptions are closed shrubland, open shrubland, and savanna ecosystems where SIF explains less than 10% of the variability in GPP for AmeriFlux sites in those ecosystems due, in part, to a low signal-to-noise ratio.

Many of the ecosystems exhibit a similar linear relationship between SIF and GPP, which begs the question: *"what ecosystems have a distinct SIF-GPP relationship?"* To address this, we bootstrap the bisquare regression for each ecosystem 2000 times. The slopes from this bootstrap can be seen in Figure 2. The range of slopes vary from 13 to 18 $\left(\mu\text{mol m}^{-2}\,\text{s}^{-1}\right)/\left(\text{mW m}^{-2}\,\text{sr}^{-1}\,\text{s}^{-1}\right)$ with grasslands at the low end and evergreen needleleaf forests at the high end. We then use a two component Gaussian mixture model (see, for example, Bishop, 2007) to identify clusters of ecosystems with a similar SIF-GPP relationship. The implementation of our Gaussian mixture model is adapted from Turner and Jacob (2015). Parameters of the mixture model are obtained via an iterative expectation-maximization algorithm. A drawback of these mixture models is they often find local minima. To address this, we repeat the fitting of the mixture model with multiple initializations and use simulated annealing to search for a global minimum. We tested a range of mixture model sizes and found a mixture of two Gaussians to be the most robust. The resulting mixture model is overlaid on the histogram in Figure 2.

We observe a clustering of ecosystems with SIF-GPP relationships around 16.3 $\left(\mu\text{mol m}^{-2}\,\text{s}^{-1}\right)/\left(\text{mW m}^{-2}\,\text{sr}^{-1}\right.$ This grouping is the dominant weighting term for wetlands, evergreen needleleaf forest, deciduous broadleaf forest, mixed forest, cropland, and woody savanna. We refer to this cluster as the "Dominant Cluster" and assume that ecosystems not specifically mentioned elsewhere will have a response that is similar to this primary cluster. The other component of the mixture model corresponds to grasslands. Table 1 lists the SIF-GPP relationships for these two clusters. These relationships can be used to reconstruct GPP

Table 1. SIF-GPP relationships for different groupings.

Cluster	SIF-GPP relationship[a] (s_i)
Dominant Cluster	16.3 ± 0.4
Grassland	13.7 ± 0.1

[a]All SIF-GPP relationships have units of $\left(\mu\text{mol m}^{-2} \text{ s}^{-1} \right) / \left(\text{mW m}^{-2} \text{ sr}^{-1} \text{ nm}^{-1} \right)$. Uncertainty is the diagonal of the covariance matrix for the mixture model.

from TROPOMI SIF as: GPP $=$ SIF $\times$ $\left(\sum_i f_i s_i \right)$ where s_i is the SIF-GPP relationship in Table 1 for the ith cluster and f_i is the fraction of a grid cell represented by that cluster.
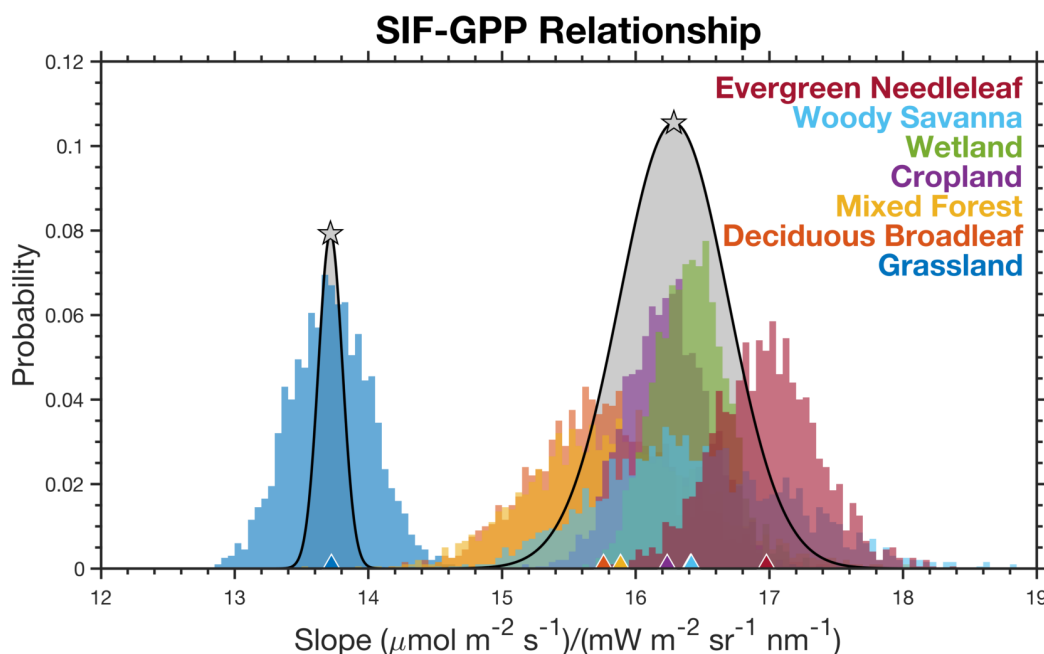
Figure 2. **Identifying distinct SIF-GPP relationships across ecosystems.** Histogram shows the distribution of slopes that map SIF to GPP using a bisquare regression and a 2000 member bootstrap. Colors denote the different ecosystems and triangles at the bottom show the mean for that ecosystem. Gray distributions are from a two-member Gaussian Mixture Model and the stars indicate the mean for that component.

TROPOMI is in low earth orbit and only observes a snapshot in time. The equatorial overpass time at nadir is 13:30 local time. By assuming that GPP scales linearly with PAR (i.e., Eq. 1) we can compute a correction factor to estimate daily integrated GPP. More formally, we scale the instantaneous SIF by the ratio of the integral of the cosine of the solar zenith angle (SZA) over the day to cos (SZA) from the TROPOMI overpass time. Putting everything together, we estimate daily GPP from TROPOMI SIF

148   observations as:

$$\text{GPP}(x,y,t) = \text{SIF}(x,y,t) \cdot \gamma \sum_i s_i f_i(x,y) \cdot \frac{\int_{t_0}^{t_f} \cos\left[\text{SZA}(x,y,t)\right] \mathrm{d}t}{\cos\left[\text{SZA}(x,y,t_s)\right]} \tag{4}$$

149   where $\text{SIF}(x,y,t)$ is the 500-m downscaled SIF using a 16-day moving window, γ is a unit
150   conversion from μmol to gC, s_i is the SIF-GPP relationship inferred from comparison
151   with AmeriFlux GPP (see Table 1), $f_i(x,y)$ is the fraction of the grid cell represented
152   by the ith cluster, SZA is the local solar zenith angle, t_0 is sunrise, t_f is sunset, and t_s
153   is the hour corresponding to the TROPOMI overpass time.

3 Drivers of interannual variations in US gross primary productivity

155   Figure 3 shows annual mean GPP across CONUS inferred from TROPOMI SIF
156   measurements using Eq. 4. A number of prominent features are visible such as the Cen-
157   tral Valley of California, the Snake River Valley in Idaho, and the Adirondack Moun-
158   tains in upstate New York. California's Central Valley and Idaho's Snake River Valley
159   are both major agricultural regions in the western US (e.g., the Central Valley of Cal-
160   iforia accounts for more than 15% of irrigated land in the US). The Adirondack Moun-
161   tains are a roughly circular dome that rise above the surrounding lowlands, resulting in
162   a shorter growing season and lower annual mean GPP. This shortened growing season
163   can be seen in an animation of GPP over CONUS (Supplemental Movie S1).

164   We observe substantial GPP across the eastern US (delineated here by 98°W) with
165   annual mean values generally in excess of 5 gC/m^2/day. This region accounts for less
166   than half of the land but more than 70% of the annual mean GPP. This delineation in
167   GPP roughly coincides with the location of drylands in CONUS that are more sensitive
168   to changes in precipitation; drylands are also projected to expand in future climate (Yao
169   et al., 2020). Most of the large year-to-year differences occur in these western US dry-
170   lands (see Fig. 3c), a notable exception being a negative GPP anomaly in 2019 relative
171   to 2018 that extended across Illinois, Indiana, and Ohio. Here we highlight four precipitation-
172   driven GPP anomalies, which taken together, account for 28% of the interannual GPP
173   variability across the United States: 1) 2018 drought in west Texas, 2) 2019 midwest-
174   ern corn belt flooding, 3) 2018 drought in South Dakota, and 4) 2018 drought in Cal-
175   ifornia. Figure 4 summarizes the interannual precipitation differences that we hypoth-
176   esize are responsible for explaining these four GPP anomalies.

177   The largest positive GPP anomaly in 2019 relative to 2018 was observed across west-
178   ern Texas. This single event accounted for 11% of the year-to-year difference in GPP across
179   CONUS. From Figure 4a, we observe 50% higher GPP in spring 2019 compared to spring
180   2018. This increase in GPP was driven by a lack of precipitation in spring 2018. The cu-
181   mulative precipitation from October 2017 through June 2018 was 50% less than Octo-
182   ber 2018 through June 2019 (500 mm vs 1000 mm). The other notable difference between
183   GPP in 2018 and 2019 was a second peak during fall 2018 that was not present in 2019.
184   This second peak coincided with a series of precipitation events beginning in early Septem-
185   ber. This tight coupling between GPP and precipitation is expected for dryland systems
186   such as west Texas (e.g., Smith et al., 2019). The seasonal GPP dynamics inferred from
187   TROPOMI SIF are also present in the MODIS vegetation index NIR$_\text{v}$, albeit with slight
188   differences in magnitude, implying convergent responses in SIF and NIR$_\text{v}$ for this ecosys-
189   tem.

190   The second largest anomaly is the reduction in 2019 GPP relative to 2018 across
191   the midwestern corn belt (defined here as Illinois, Indiana, and Ohio) that accounted for
192   7% of the year-to-year difference in CONUS GPP. We observe a decrease in the max-
193   imum GPP between 2019 and 2018 as well as a two week delay in the timing of the max-
194   imum. This anomaly was highlighted in recent work from Yin et al. (2020) who attribute
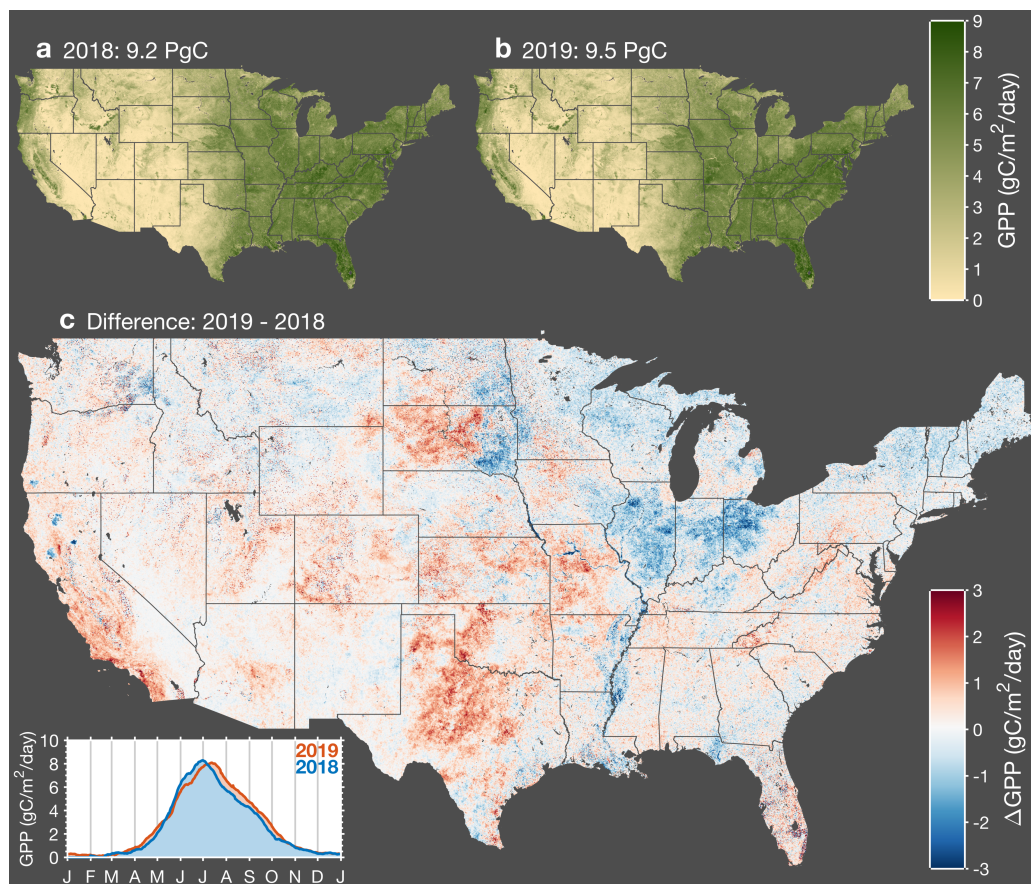195   the anomaly to flooding in the midwestern US. The flooding delayed planting of crops

Figure 3.   Interannual variations in gross primary productivity across CONUS.
Map of annual mean GPP for 2018 (panel a) and 2019 (panel b). (Panel c) Map of the difference in annual mean GPP between 2019 and 2018. Red indicates higher GPP in 2019 and red indicates higher GPP in 2018. Inset in bottom left corner shows a timeseries of the average GPP across CONUS for 2018 and 2019.
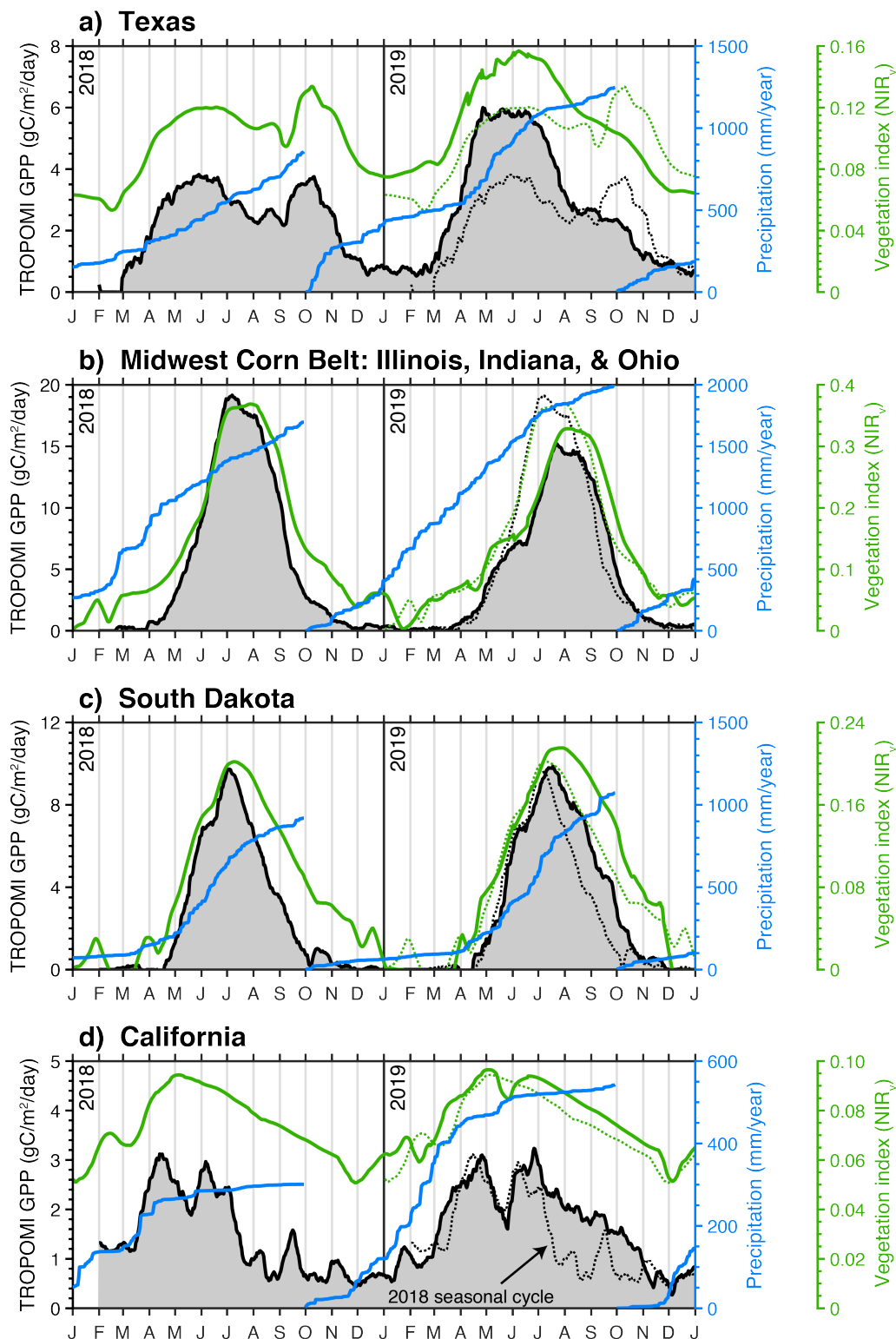
Figure 4. **Major drivers of interannual variability in CONUS GPP.** Black line shows the TROPOMI-derived GPP over Texas (a), the midwest corn belt (b), South Dakota (c), and California (d). Blue line shows the cumulative precipitation over the water year as measured by the GPM satellite. Green line is NIR_v from MODIS. Black and Green dotted lines are 2018 GPP and NIR_v superimposed on the 2019 timeseries.

by two weeks and resulted in decreased carbon uptake across the midwestern corn belt and Mississippi Alluvial Valley, where we also observe a negative anomaly in Figure 3c. Yin et al. (2020) provide a detailed discussion of these floods and their impacts on crop productivity.

South Dakota exhibits a dipole with positive anomalies in 2019 in the west and negative anomalies in the east, again relative to 2018. The negative anomalies in the east are driven by the flooding events discussed above and in Yin et al. (2020). However, the positive anomaly in western portion of the state is the dominant term. This positive anomaly is driven by a series of summer precipitation events that served to extend the growing season across the western plains. From Figure 4c, we can see three precipitation events throughout the mid-to-late summer that coincide with pauses in senesence: mid-July, early August, and mid-September. As with Texas, this highlights the tight coupling between GPP and precipitation for dryland systems. In toto, these precipitation events served to increase statewide GPP in 2019 relative to 2018.

The final notable anomaly is California's positive GPP anomaly in 2019. 2018 was a mild drought in California with $\sim$80% of the state being classified as abnormally dry; 2019 had 50% more precipitation during the water year than 2018 (Figure 4c). Two consequences of this drought in 2018 were: a delayed onset of photosynthesis and a mid-summer senescence. The onset of photosynthesis in 2018 coincided with a series of atmospheric rivers that delivered about a third of the total precipitation that year, indicating a water limitation up to that point. In contrast, 2019 had ample precipitation through the winter and we observe both an earlier onset of photosynthesis and an extension of the growing season into the fall. Evergreen forests are the main contributor to the SIF signal during the summer and fall (Turner et al., 2020) and, as such, will be more sensitive to the accumulated precipitation. The spatial pattern of the differences in August-November GPP (Fig. S3) strongly correlate with evergreen forests.

In contrast to the anomalies presented earlier, the SIF-derived GPP and MODIS-based vegetation index (NIR_v) show divergent seasonal dynamics for California. NIR_v shows small differences between 2018 and 2019 with a strong similarity to the 2019 SIF-derived GPP. Vegetation indices estimate *photosynthetic capacity* provided optimal soil moisture, temperature, and PAR are known (Sellers, 1985). As such, this suggests that we observed a down-regulation of photosynthesis from evergreen forests in response to a water limitation during fall 2018, whereas these forests were close to photosynthetic capacity in fall 2019 resulting in a similar seasonality to 2018 and 2019 NIR_v. Sims et al. (2014) also report a low sensitivity of MODIS vegetation indices to drought stress in forests.

4 Conclusions

We have developed a parsimonious relationship between measurements of SIF from TROPOMI and GPP inferred from flux towers. This relationship allows for estimation of GPP directly from TROPOMI SIF measurements. We combine this SIF-GPP relationship with work downscaling TROPOMI data to 500-m spatial resolution to construct estimates of GPP across the conterminous United States in 2018 and 2019. Our estimate of US GPP varies by less than 4% between 2018 and 2019. We do, however, observe large regional anomalies that are driven by extreme precipitation events. Namely, west Texas, South Dakota, and California experienced droughts in 2018 while the midwestern US corn belt states (Illinois, Indiana, and Ohio) experienced flooding in 2019. Taken together, these four events account for 28% of the year-to-year variability in GPP across the conterminous United States.

The impact of the west Texas drought, South Dakota drought, and midwestern flooding are observed in other remote-sensing measures of photosynthetic capacity such as NIR_v

while the California drought shows a divergent result using SIF; the divergent responses
are driven by specific ecosystems such as evergreen forests. Our work suggests that SIF
provides a measure of *photosynthetic activity* as opposed to *photosynthetic capacity*, and
converge with other remote-sensing measures under non-stressed conditions. Future work
investigating the response to extreme events across ecosystems may provide additional
insight into these divergent responses in remote-sensing measurements related to pho-
tosynthesis.

Acknowledgments

References

Badgley, G., Anderegg, L. D. L., Berry, J. A., & Field, C. B. (2019). Terrestrial
Gross Primary Production: Using NIR$_V$ to Scale from Site to Globe. *Global
change biology*. doi: 10.1111/gcb.14729

Badgley, G., Field, C. B., & Berry, J. A. (2017). Canopy near-infrared reflectance
and terrestrial photosynthesis. *Sci Adv*, *3*(3), e1602244. doi: 10.1126/sciadv
.1602244

Baldocchi, D., Falge, E., Gu, L., Olson, R., Hollinger, D., Running, S., ... Wofsy,
S. (2001). FLUXNET: A New Tool to Study the Temporal and Spatial Vari-
ability of Ecosystem–Scale Carbon Dioxide, Water Vapor, and Energy Flux
Densities. *Bulletin of the American Meteorological Society*, *82*(11), 2415-2434.
doi: 10.1175/1520-0477(2001)082⟨2415:fantts⟩2.3.co;2

Baldocchi, D. D., Hicks, B. B., & Meyers, T. P. (1988). Measuring Biosphere-
Atmosphere Exchanges of Biologically Related Gases with Micrometeorological

297   Methods. *Ecology*, *69*(5), 1331-1340. doi: 10.2307/1941631

298 Bishop, C. M.   (2007).   *Pattern Recognition and Machine Learning* (1st ed.).
299   Springer.

300 Butterfield, Z., Buermann, W., & Keppel-Aleks, G. (2020). Satellite observations re-
301   veal seasonal redistribution of northern ecosystem productivity in response to
302   interannual climate variability.   *Remote Sensing of Environment*, *242*, 111755.
303   doi: 10.1016/j.rse.2020.111755

304 Dechant, B., Ryu, Y., Badgley, G., Zeng, Y., Berry, J. A., Zhang, Y., . . . Moya, I.
305   (2020). Canopy structure explains the relationship between photosynthesis and
306   sun-induced chlorophyll fluorescence in crops. *Remote Sensing of Environment*,
307   *241*, 111733. doi: 10.1016/j.rse.2020.111733

308 Frankenberg, C., Butz, A., & Toon, G. C.   (2011).   Disentangling chlorophyll fluo-
309   rescence from atmospheric scattering effects in O_2A-band spectra of reflected
310   sun-light. *Geophysical Research Letters*, *38*(3). doi: 10.1029/2010gl045896

311 Guanter, L., Zhang, Y., Jung, M., Joiner, J., Voigt, M., Berry, J. A., . . . Griffis,
312   T. J.   (2014).   Global and time-resolved monitoring of crop photosynthe-
313   sis with chlorophyll fluorescence.   *Proceedings of the National Academy*
314   *of Sciences of the United States of America*, *111*(14), E1327-33.   doi:
315   10.1073/pnas.1320008111

316 Köhler, P., Frankenberg, C., Magney, T. S., Guanter, L., Joiner, J., & Landgraf, J.
317   (2018).   Global Retrievals of Solar-Induced Chlorophyll Fluorescence With
318   TROPOMI: First Results and Intersensor Comparison to OCO-2.   *Geophysical*
319   *Research Letters*, *45*(19), 10,456-10,463. doi: 10.1029/2018gl079031

320 Lee, J. E., Frankenberg, C., van der Tol, C., Berry, J. A., Guanter, L., Boyce, C. K.,
321   . . . Saatchi, S. (2013). Forest productivity and water stress in Amazonia: ob-
322   servations from GOSAT chlorophyll fluorescence.   *Proc. Biol. Sci.*, *280*(1761),
323   20130171. doi: 10.1098/rspb.2013.0171

324 Le Quéré, C., Andrew, R. M., Friedlingstein, P., Sitch, S., Hauck, J., Pongratz, J.,
325   . . . Zheng, B.   (2018).   Global Carbon Budget 2018.   *Earth System Science*
326   *Data*, *10*(4), 2141-2194. doi: 10.5194/essd-10-2141-2018

327 Magney, T. S., Bowling, D. R., Logan, B. A., Grossmann, K., Stutz, J., Blanken,
328   P. D., . . . Frankenberg, C.   (2019).   Mechanistic evidence for tracking the
329   seasonality of photosynthesis with solar-induced fluorescence.   *Proceedings of*
330   *the National Academy of Sciences of the United States of America*, *116*(24),
331   11640-11645. doi: 10.1073/pnas.1900278116

332 Marrs, J. K., Reblin, J. S., Logan, B. A., Allen, D. W., Reinmann, A. B., Bombard,
333   D. M., . . . Hutyra, L. R.   (2020).   SolarInduced Fluorescence Does Not Track
334   Photosynthetic Carbon Assimilation Following Induced Stomatal Closure.
335   *Geophysical Research Letters*, *47*(15). doi: 10.1029/2020gl087956

336 Monteith, J. L.   (1972).   Solar Radiation and Productivity in Tropical Ecosystems.
337   *Journal of Applied Ecology*, *9*(3), 747-766.

338 Parazoo, N. C., Bowman, K., Fisher, J. B., Frankenberg, C., Jones, D. B., Cescatti,
339   A., . . . Montagnani, L.   (2014).   Terrestrial gross primary production inferred
340   from satellite fluorescence and vegetation models.   *Global change biology*,
341   *20*(10), 3103-21. doi: 10.1111/gcb.12652

342 Reichstein, M., Falge, E., Baldocchi, D., Papale, D., Aubinet, M., Berbigier, P., . . .
343   Valentini, R.   (2005).   On the separation of net ecosystem exchange into as-
344   similation and ecosystem respiration: review and improved algorithm.   *Global*
345   *change biology*, *11*(9), 1424-1439. doi: 10.1111/j.1365-2486.2005.001002.x

346 Schaaf, C. B., Gao, F., Strahler, A. H., Lucht, W., Li, X., Tsang, T., . . . Roy,
347   D.   (2002).   First operational BRDF, albedo nadir reflectance products
348   from MODIS.   *Remote Sensing of Environment*, *83*(1-2), 135-148.   doi:
349   10.1016/s0034-4257(02)00091-3

350 Sellers, P. J.   (1985).   Canopy reflectance, photosynthesis and transpira-
351   tion.   *International Journal of Remote Sensing*, *6*(8), 1335-1372.   doi:

10.1080/01431168508948283

Sims, D. A., Brzostek, E. R., Rahman, A. F., Dragoni, D., & Phillips, R. P. (2014). An improved approach for remotely sensing water stress impacts on forest C uptake. *Global change biology*, *20*(9), 2856-2866. doi: 10.1111/gcb.12537

Smith, W. K., Dannenberg, M. P., Yan, D., Herrmann, S., Barnes, M. L., Barron-Gafford, G. A., . . . Yang, J. (2019). Remote sensing of dryland ecosystem structure and function: Progress, challenges, and opportunities. *Remote Sensing of Environment*, *233*, 111401. doi: 10.1016/j.rse.2019.111401

Sun, Y., Frankenberg, C., Jung, M., Joiner, J., Guanter, L., Köhler, P., & Magney, T. (2018). Overview of Solar-Induced chlorophyll Fluorescence (SIF) from the Orbiting Carbon Observatory-2: Retrieval, cross-mission comparison, and global monitoring for GPP. *Remote Sensing of Environment*, *209*, 808-823. doi: 10.1016/j.rse.2018.02.016

Sun, Y., Frankenberg, C., Wood, J. D., Schimel, D. S., Jung, M., Guanter, L., . . . Yuen, K. (2017). OCO-2 advances photosynthesis observation from space via solar-induced chlorophyll fluorescence. *Science*, *358*(6360). doi: 10.1126/science.aam5747

Sun, Y., Fu, R., Dickinson, R., Joiner, J., Frankenberg, C., Gu, L., . . . Fernando, N. (2015). Drought onset mechanisms revealed by satellite solar-induced chlorophyll fluorescence: Insights from two contrasting extreme events. *Journal of Geophysical Research: Biogeosciences*, *120*(11), 2427-2440. doi: 10.1002/2015jg003150

Turner, A. J., & Jacob, D. J. (2015). Balancing aggregation and smoothing errors in inverse models. *Atmos Chem Phys*, *15*(12), 7039-7048. doi: 10.5194/acp-15 -7039-2015

Turner, A. J., K¨hler, P., Magney, T. S., Frankenberg, C., Fung, I., & Cohen, R. C. (2020). A double peak in the seasonality of California's photosynthesis as observed from space. *Biogeosciences*, *17*(2), 405-422. doi: 10.5194/bg-17-405-2020

USDA. (2018). *National Agricultural Statistics Service Cropland Data Layer: Published crop-specific data layer.* Retrieved 15/3/2019, from https://nassgeodata.gmu.edu/CropScape/

Veefkind, J. P., Aben, I., McMullan, K., Förster, H., de Vries, J., Otter, G., . . . Levelt, P. F. (2012). TROPOMI on the ESA Sentinel-5 Precursor: A GMES mission for global observations of the atmospheric composition for climate, air quality and ozone layer applications. *Proc SPIE*, *120*, 70-83. doi: 10.1016/j.rse.2011.09.027

Wang, X., Dannenberg, M. P., Yan, D., Jones, M. O., Kimball, J. S., Moore, D. J. P., . . . Smith, W. K. (2020). Globally Consistent Patterns of Asynchrony in Vegetation Phenology Derived From Optical, Microwave, and Fluorescence Satellite Data. *Journal of Geophysical Research: Biogeosciences*, *125*(7). doi: 10.1029/2020jg005732

Yang, H., Yang, X., Zhang, Y., Heskel, M. A., Lu, X., Munger, J. W., . . . Tang, J. (2017). Chlorophyll fluorescence tracks seasonal variations of photosynthesis from leaf to canopy in a temperate forest. *Global change biology*, *23*(7), 2874-2886. doi: 10.1111/gcb.13590

Yang, X., Tang, J., Mustard, J. F., Lee, J.-E., Rossini, M., Joiner, J., . . . Richardson, A. D. (2015). Solar-induced chlorophyll fluorescence that correlates with canopy photosynthesis on diurnal and seasonal scales in a temperate deciduous forest. *Geophysical Research Letters*, *42*(8), 2977-2987. doi: 10.1002/2015gl063201

Yao, J., Liu, H., Huang, J., Gao, Z., Wang, G., Li, D., . . . Chen, X. (2020). Accelerated dryland expansion regulates future variability in dryland gross primary production. *Nature communications*, *11*(1). doi: 10.1038/s41467-020-15515-2

Yin, Y., Byrne, B., Liu, J., Wennberg, P. O., Davis, K. J., Magney, T., . . . Franken-

407   berg, C.   (2020).   Cropland Carbon Uptake Delayed and Reduced by 2019
408   Midwest Floods. *AGU Advances*, *1*(1). doi: 10.1029/2019av000140